Table 1 Inherent accuracy of the motion correction system in the two PET scanners

Scanner	$T_{G\to S}$						$T_{S\to P}$				# of point positions
	Rotational angle (deg)			Translation (mm)			e_x	e_y	e_z	RMSE	
	r_x	r_y	r_z	t_x	t_y	t_z					
ECAT EXACT HR	0.0	0.0	0.0	0.0	0.0	0.0	0.0 ± 0.8	0.0 ± 0.9	0.0 ± 0.8	1.3 ± 0.4	10
HEADTOME-V	0.0	0.0	0.0	0.0	0.0	0.1	0.0 ± 1.5	0.0 ± 1.6	0.0 ± 0.6	2.3 ± 0.2	14

Standard deviations of rotational angles and translations obtained from $T_{G\to S}$ data and approximation errors (mean ± SD in mm) by transforming positions of a point source from the POLARIS coordinate to the PET coordinate using $T_{S\to P}$. Columns $T_{G\to S}$, r_x, r_y and r_z denote SDs of rotational angles about three orthogonal X, Y, and Z axes, respectively. t_x, t_y and t_z denote SDs of translations along three orthogonal axes, respectively. Columns $T_{S\to P}$, e_x, e_y, and e_z denote average values (mean ± SD in mm) of $e(i, X)$, $e(i, Y)$, and $e(i, Z)$, respectively. $e(i, k)$ was defined in Eq. 4. *RMSE* denotes an average value (mean ± SD in mm) of $RMSE(i)$, defined in Eq. 5

Table 2 The observed misalignment and correlation coefficients for the phantom study

Scan no.	Rotation (deg)			Translation (mm)			Correlation coefficient	
	r_x	r_y	r_z	t_x	t_y	t_z	Before MC	After MC
2	0.0	0.2	5.1	35.7	0.8	−3.4	0.896	0.997
3	0.0	−1.0	1.3	0.9	35.2	3.2	0.938	0.995
4	0.0	−0.2	0.9	5.9	0.1	42.8	0.917	0.971
5	13.1	1.4	0.4	1.9	22.5	17.1	0.926	0.986
6	2.4	−15.6	−2.1	10.9	3.8	4.7	0.938	0.982
7	−0.6	1.8	−13.5	13.4	11.9	−9.5	0.960	0.992

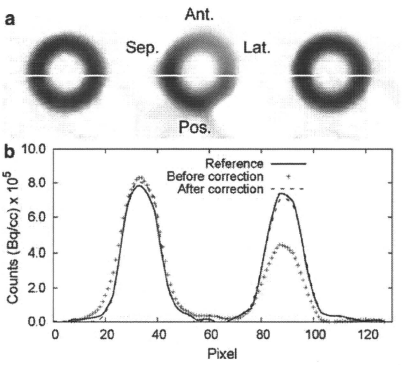

Fig. 3 Reconstructed and reoriented images of the phantom. **a** Reconstructed images. *Left*, *mid*, and *right* columns represent the reference emission image (no misalignment), the second emission images before correction for misalignment, and the second emission images after correction for the misalignment, respectively. **b** Profiles at the level of white lines in images. *Solid line*, *cross symbols*, and *dashed lines* represent the first emission image, the second emission images before correction, and the second emission images after correction, respectively

effects of our correction technique are demonstrated in Fig. 3. The left column in Fig. 3a is the reference emission image (no misalignment). The middle and right columns represent the emission images with the misalignment of the X-direction before and after the corrections. For the image in the middle column, only the position was transformed to the transmission coordinate after the reconstruction. Figure 3b represents line profiles at the level of white lines in the slices.

Human study

Table 3 summarizes the observed movements of the subject during scans relative to the beginning of the first transmission scan, in the form of rotational angles about and translations along three orthogonal axes. It was observed that the magnitude of the average parts of the rotational angles and translations tended to increase. The value of t_z changed from -1.8 ± 0.6 to 28.3 ± 0.6 mm between the ^{15}O-water emission and the second transmission scan mainly because of the 30-mm shift of the couch as well as the motions of the subject. There was little change in the SD in any rotational angle or translation among the scans.

Figure 4 shows motion parameters during ^{15}O-water scan. Figure 4a and b represent the sample-by-sample and frame-averaged translations. Figure 4c and d shows the sample-by-sample and frame-averaged rotational angles.

Table 4 shows that the MBF values (mean ± SD), which were obtained from nine myocardial segments, were 0.94 ± 0.12, 0.91 ± 0.13, 1.03 ± 0.21, and 0.93 ± 0.11 mL/min/g for the four cases. The values for cases 1 and 2 were obtained from the emission data and the first attenuation map before and after motion correction. The values for cases 3 and 4 were obtained from the emission data and the second attenuation map before and after the corrections for the subject's motions and the 30-mm shift of the couch. There were significant

Table 3 Observed movements (mean ± SD) of the healthy volunteer during scans relative to the beginning of the first transmission scan

Scan	Rotational angle (deg)			Translation (mm)		
	r_x	r_y	r_z	t_x	t_y	t_z
TCT 1	−0.1 ± 0.2	−0.4 ± 0.2	−0.2 ± 0.2	0.7 ± 0.5	1.3 ± 0.6	1.0 ± 0.8
$C^{15}O$	0.0 ± 0.2	−0.1 ± 0.2	−0.7 ± 0.1	2.6 ± 0.3	1.0 ± 0.5	−1.7 ± 0.7
^{15}O-water	0.4 ± 0.2	0.0 ± 0.1	−0.7 ± 0.1	2.7 ± 0.2	1.3 ± 0.4	−1.8 ± 0.6
TCT 2	−0.4 ± 0.2	0.7 ± 0.2	−2.0 ± 0.1	3.7 ± 0.3	2.6 ± 0.5	28.3 ± 0.6

r_x, r_y, and r_z denote rotational angles (degrees) about X, Y, and Z-axes, respectively. t_x, t_y, and t_z denote translations (mm) along X, Y, and Z axes, respectively

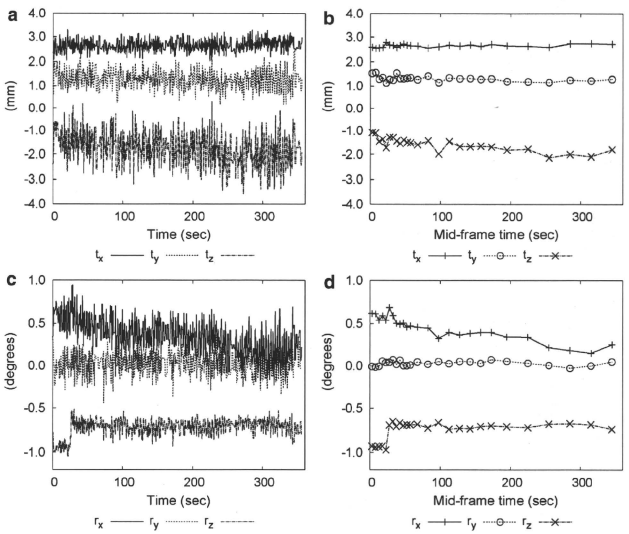

Fig. 4 Motion parameters during ^{15}O-water study on the healthy volunteer. **a**, **b** Sample-by-sample and frame-averaged translations. **c**, **d** Sample-by-sample and frame-averaged rotational angles

Table 4 MBF values (mL/min/g of perfusable tissue) of the healthy volunteer

Myocardial region	Case			
	1	2	3	4
Apical	1.05	1.00	0.99	1.05
Mid-anterior	0.92	0.89	1.26	0.99
Mid-lateral	0.93	0.89	1.38	0.89
Mid-posterior	1.14	1.16	0.96	1.01
Mid-septal	1.05	1.06	1.08	1.12
Basal-anterior	0.87	0.80	1.18	0.80
Basal-lateral	0.86	0.82	0.95	0.84
Basal-posterior	0.88	0.83	0.84	0.86
Basal-septal	0.73	0.72	0.65	0.82
Mean ± SD	0.94 ± 0.12	0.91 ± 0.13	1.03 ± 0.21	0.93 ± 0.11

differences in the mid-anterior and mid-lateral regions as well as the basal-anterior regions between cases 1 and 3.

Figure 5 demonstrates the influence of misalignment between an attenuation map and emission data on the quality of myocardial images, as well as the effect of our correction technique. Figure 5a–f represent the build-up and washout phase images of middle myocardial obtained from the ^{15}O-water data. Anterior, lateral, posterior, and septal regions of myocardia were arranged in a clockwise manner. Figure 5a and e was obtained from the data of case 1, and Fig. 5b and f was calculated from the data obtained in case 2. Figure 5c and g was derived from the data in case 3, and only positions of reconstructed images were transformed to the first transmission coordinate after reconstructions for visual

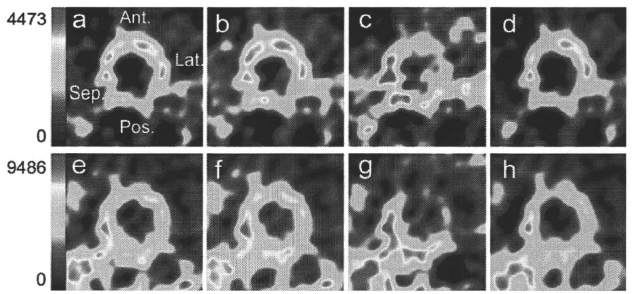

Fig. 5 Myocardial images of the healthy volunteer. **a–d** Build-up phase images. **e–h** Washout phase images. **a** and **e** were reference images obtained from data of case 1. **b** and **f** are images from data of case 2, which were corrected for the motions of the subject. **c** and **g** are images from case 3 of the emission data and the second attenuation map without our motion corrections. **d** and **h** are images from case 4, which were corrected for the motions and the misalignment between the emission data and the second attenuation map

comparison with the other images. Figure 5c and g demonstrates that reconstruction with an incorrect attenuation map caused spurious defects from anterior to lateral myocardial regions, as well as an artifact in the posterior region. Figure 5d and h is an image calculated from data obtained in case 4, in which images were also transformed to the first transmission coordinate.

Discussion

In this paper, we developed an optical motion-tracking based system to detect global movement of the subject and correct for the movement during cardiac ^{15}O-water studies.

First, the inherent accuracy of the system was assessed from position calibrations. As shown in Table 1, the $T_{G\to S}$ part could be negligibly small compared with the magnitude of the subject's motions in Table 3 and Fig. 4. For the $T_{S\to P}$ part shown in Table 1, there was no bias in any direction. The value of RMSE for each scanner was smaller than the spatial resolution of the scanner [21, 22]. Therefore, it was considered that the position calibrations provided a sufficient level of accuracy for our motion corrections.

To validate the present technique, we performed a cardiac phantom study. As shown in Fig. 3a, a defect and blurred region from the anterior to the lateral, which was mainly caused by a 5.1° rotation about the Z axis and a 35.7 mm shift along the X axis, was recovered using the present technique. The effect of the present technique was also shown more objectively by the correlation coefficients and profile comparison in Fig. 3b.

In the healthy volunteer study, no correction was applied for the motions of the subjects during the transmission scans because the PET scanners do not have the ability to perform dynamic transmission scans. Motions during a transmission scan resulted in a blurred attenuation map, and caused over- or under-estimation of the radioactive concentration in myocardium of ^{15}O-water images. However, as shown in Table 3, the magnitudes of the mean and SD during the transmission scans were smaller than the spatial resolution provided by the PET scanner, even if the magnitudes were slightly larger than those of the mean and SD during emission scans. In addition, a 9-mm smoothing filter was employed during the image reconstruction stage. Therefore, we considered that valid transmission data were acquired for the subject. For the same reason as in the case of the transmission data, the emission data of ^{15}O-water scan were acquired properly. So we used the data of case 1 as the reference for the other cases.

The global movement and cyclic movement of the target were observed as shown in Fig. 4a and c. The cyclic movement was attributed to respiration. From Fig. 4b and d, the cyclic movement was smoothed by frame-averaging. In addition, the regional MBF values (Table 4) and the myocardial images (Fig. 5) of cases 1 and 2, which were derived from the same transmission and emission scans before and after the motion correction, were nearly the same. This result indicated that our system provided reasonably accurate information about the global movement.

In case 3, in which no correction for the subject's motions and the 30-mm shift between the emission data and the second attenuation map was applied, the MBF values for the mid-anterior, mid-lateral, and basal-anterior regions were

significantly larger than the reference values. This overestimation was associated with spurious defects from the anterior to lateral regions, as shown in Fig. 5c and g. In case 4 with our correction technique, the MBF values for myocardial regions, in which overestimated MBFs were obtained for the corresponding regions in case 3, were similar to the reference values. The image quality in Fig. 5d and h was also nearly the same as in Fig. 5a and e. Figure 5d shows a clearly delineated contour of the myocardial region similar to the contour in Fig. 5a. The spurious defects from the anterior to lateral regions in Fig. 5g were recovered in Fig 5h. Owing to these results, the present technique tracked the location of the external target attached to the chest skin accurately, and then corrected the artificial misalignment during transmission and emission scans. Figure 5 not only shows the effects of our correction technique, but also suggests that the use of an attenuation map with large global movement could cause the appearance of spurious defects in myocardial imaging with ^{15}O-water PET.

Several listmode-based motion correction techniques have hitherto been proposed [1, 3–7]. Compared to these techniques, our technique provides poorer time resolution, even though our technique was applied to an emission scan consisting of dynamic frames with shorter duration. Listmode-based methods, however, require wide band transmission and high computational power for manipulating the listmode event data, especially under high count rates. For the listmode-based methods, in which data processing is conducted prior to the motion correction, corrections for detector efficiency, detector geometry, and crystal interferences are important issues, especially in the case of scanners with gaps between detectors or no intersection of motion-corrected LOR with detector(s). For our technique with 2D acquisition mode, the sinogram data are simply normalized by the built-in software of the used PET scanners. Our technique could shorten the processing time by re-binning the listmode data during the period when substantial movement is detected, and then correcting the re-framed dynamic sinogram. Furthermore, our technique is applicable to many commercially available PET scanners, which often have no feasibility of listmode acquisition.

Instead fixating the POLARIS on a certain position, such as the gantry of the PET scanner described in [3, 6], we attached the reference target onto the gantry and then used the target and the calibration tool to transform the subject's position from the POLARIS coordinate to the PET coordinate. Thus, our method allows for more flexibility in adjusting with regard to the location of the POLARIS. This is an important feature for the cardiac study due to the large inter-subject variability in the shapes of the torsos among patients, and as shown in Fig. 1e, there were enough gaps to set the best positioning for cardiac PET study. However, for exercise study, such as the studies with cycling, smaller targets and supporting post might be needed to ensure working space. An additional advantage is the portability of the POLARIS, which enables the sharing of the device among scanners in different locations.

For our technique based on the rigid body model, two targets were enough to detect the displacements and rotations of the thoraxes of the subjects, in which the secondary target was used as a reserve for cases in which the primary target was hidden from the FOV of the POLARIS. The secondary target and additional targets might be used with the corporation of the primary target to construct a non-rigid body model by detecting deformation between the chest and abdomen, and/or over the thorax region.

Another approach for the motion correction was based on image-driven information. Juslin et al. proposed an alignment technique for dynamic ^{15}O-water PET images by means of the independent component analysis. They demonstrated an improvement in quantitatively functional and parametric values, although they did not take into account for the misregistration between the transmission and emission data sets, and the movements during each emission scan [24]. The advantages of our method comparing software-based technique were (1) the misalignment between the transmission and dynamic image, and misalignment among the dynamic images could be corrected because our method was independent of the distribution and concentration of the tracer, and suboptimal image qualities (e.g., statistical noise, blurring and types of tracers). (2) Accurate attenuation correction was available because the misalignment between the transmission and the dynamic image was corrected in the reconstruction stage of the dynamic image, and (3) inherent accuracy could be obtained from the position calibration and the optical motion tracking device. Consequently, the present technique can be utilized in PET studies with several types of tracers such as ^{13}N-Ammonia and ^{18}F-FDG.

In this study, the motion correction system was demonstrated on one subject at rest. The system is to be evaluated by large population of various subjects because characteristics of motion such as magnitudes, frequencies, and directions could be different among subjects. Validation of our system is also needed for the studies during the physiologically or pharmacologically stressed conditions, in which repositioning of the heart in thoracic cavity, and larger and/or irregular (non-cyclic) chest motion by respiration would be expected. In our method, one of the limitations was correction for the misalignment due to the motion of the diaphragm with a deep breathing during a stress study, and due to the motion of the diaphragm with cough or sneezing even though during a resting study. To correct such misalignment, detection of irregular motion and a non-linear model might be needed to estimate the

location of the heart using information obtained from the locations of targets on the chest.

Our system intended to correct global movement during dynamic scans. It was expected that the system would work on transmission and emission data smoothed temporally and spatially. Attenuation correction artefacts due to respiration was out of the scope for our system, which were investigated in the X-ray combined PET system studies [25, 26].

Conclusion

Our technique using an optical motion-tracking device provided the reasonable information for correcting the global movement of the subject. It was shown that this system was applicable to detect and correct subject movement in cardiac PET studies at rest. We conclude that the present technique would contribute to improvement in the quantification of MBF in ^{15}O-water PET studies.

Acknowledgments This study was supported by a grant from New Energy and Industrial Technology Development Organization (NEDO) of Japan, the Budget for Nuclear Research of the Ministry of Education, Culture, Sports, Science and Technology (MEXT) of Japan, the Program for Promotion of Fundamental Studies in Health Science of the Organization for Pharmaceutical Safety and Research of Japan, Health Science Research Grant from the Ministry of Health, Labour and Welfare of Japan, a Grant-in-Aid for Young Scientists of the MEXT (B) (19700397) of Japan, and also a research grant for Advanced Medical Technology from the Ministry of Health, Labour and Welfare (MHLW) of Japan.

References

1. Menke M, Atkins MS, Buckley KR. Compensation methods for head motion detected during PET imaging. IEEE Trans Nucl Sci. 1996;43:310–7.
2. Picard Y, Thompson CJ. Motion correction of PET images using multiple acquisition frames. IEEE Trans Med Imaging. 1997;16:137–44.
3. Lopresti BJ, Russo A, Jones WF, Fisher T, Crouch D, Altenburger DE, et al. Implementation and performance of an optical motion tracking system for high resolution brain PET imaging. IEEE Trans Nucl Sci. 1999;46:2059–67.
4. Watabe H, Sato N, Kondoh Y, Fulton RR, Iida H. Correction of head movement using optical motion tracking system during PET study with rhesus monkey. In: Brain Imaging Using PET. San Diego: Academic Press; 2002. p. 1–8.
5. Fulton RR, Meikle SR, Eberl S, Pfeiffer J, Constable CJ. Correction for head movements in positron emission tomography using an optical motion-tracking system. IEEE Trans Nucl Sci. 2002;49:116–23.
6. Bloomfield PM, Spinks TJ, Reed J, Schnorr L, Westrip AM, Livieratos L, et al. The design and implementation of a motion correction scheme for neurological PET. Phys Med Biol. 2003;48:959–78.
7. Woo SK, Watabe H, Yong C, Kim KM, Choon C, Bloomfield PM, et al. Sinogram-based motion correction of PET images using optical motion tracking system and list-mode data acquisition. IEEE Trans Nucl Sci. 2004;51:782–8.
8. McCord ME, Bacharach SL, Bonow RO, Dilsizian V, Cuocolo A, Freedman N. Misalignment between PET transmission and emission scans: its effect on myocardial imaging. J Nucl Med. 1992;33:1209–14.
9. Germano G, Chua T, Kavanagh PB, Kiat H, Berman DS. Detection and correction of patient motion in dynamic and static myocardial SPECT using a multi-detector camera. J Nucl Med. 1993;34:1349–55.
10. Cooper JA, Neumann PH, McCandless BK. Detection of patient motion during tomographic myocardial perfusion imaging. J Nucl Med. 1993;34:1341–8.
11. Bacharach SL, Douglas MA, Carson RE, Kalkowski PJ, Freedman NM, Perrone-Filardi P, et al. Three-dimensional registration of cardiac positron emission tomography attenuation scans. J Nucl Med. 1993;34:311–21.
12. Iida H, Kanno I, Takahashi A, Miura S, Murakami M, Takahashi K, et al. Measurement of absolute myocardial blood flow with $H_2^{15}O$ and dynamic positron-emission tomography. Strategy for quantification in relation to the partial-volume effect. Circulation 1988;78:104–15 (erratum in: Circulation 1988;78:1078).
13. Iida H, Rhodes CG, de Silva R, Yamamoto Y, Araujo LI, Maseri A, et al. Myocardial tissue fraction–correction for partial volume effects and measure of tissue viability. J Nucl Med. 1991;32:2169–75.
14. Knaapen P, Boellaard R, Götte MJ, van der Weerdt AP, Visser CA, Lammertsma AA, et al. The perfusable tissue index: a marker of myocardial viability. J Nucl Cardiol. 2003;10:684–91.
15. de Silva R, Yamamoto Y, Rhodes CG, Iida H, Nihoyannopoulos P, Davies GJ, et al. Preoperative prediction of the outcome of coronary revascularization using positron emission tomography. Circulation. 1992;86:1738–42.
16. Knaapen P, Boellaard R, Götte MJ, Dijkmans PA, van Campen LM, de Cock CC, et al. Perfusable tissue index as a potential marker of fibrosis in patients with idiopathic dilated cardiomyopathy. J Nucl Med. 2004;45:1299–304.
17. Chareonthaitawee P, Kaufmann PA, Rimoldi O, Camici PG. Heterogeneity of resting and hyperemic myocardial blood flow in healthy humans. Cardiovasc Res. 2001;50:151–61.
18. Yamamoto Y, de Silva R, Rhodes CG, Araujo LI, Iida H, Rechavia E, et al. A new strategy for the assessment of viable myocardium and regional myocardial blood flow using 15O-water and dynamic positron emission tomography. Circulation. 1992;86:167–78.
19. Iida H, Rhodes CG, de Silva R, Araujo LI, Bloomfield PM, Lammertsma AA, et al. Use of the left ventricular time-activity curve as a noninvasive input function in dynamic oxygen-15-water positron emission tomography. J Nucl Med. 1992;33:1669–77.
20. Naum A, Laaksonen MS, Tuunanen H, Oikonen V, Teräs M, Kemppainen J, et al. Motion detection and correction for dynamic (15)O-water myocardial perfusion PET studies. Eur J Nucl Med Mol Imaging. 2005;32:1378–83.
21. Iida H, Miura S, Kanno I, Ogawa T, Uemura K. A new PET camera for noninvasive quantitation of physiological functional parametric images: HEADTOME-V-Dual. In: Quantification of brain function using PET. San Diego: Academic Press; 1996. 57–61.
22. Wienhard K, Dahlbom M, Eriksson L, Michel C, Bruckbauer T, Pietrzyk U, et al. The ECAT EXACT HR: performance of a new high resolution positron scanner. J Comput Assist Tomogr. 1994;18:110–8.

23. Iida H, Rhodes CG, Araujo LI, Yamamoto Y, de Silva R, Maseri A, et al. Noninvasive quantification of regional myocardial metabolic rate for oxygen by use of $^{15}O_2$ inhalation and positron emission tomography. Theory, error analysis, and application in humans. Circulation. 1996;94:792–807.
24. Juslin A, Lötjönen J, Nesterov SV, Kalliokoski K, Knuuti J, Ruotsalainen U. Alignment of 3-dimensional cardiac structures in O-15-labeled water PET emission images with mutual information. J Nucl Cardiol. 2007;1:82–91.
25. McQuaid SJ, Hutton BF. Sources of attenuation-correction artefacts in cardiac PET/CT and SPECT/CT. Eur J Nucl Med Mol Imaging. 2008;35:1117–23.
26. Gould KL, Pan T, Loghin C, Johnson NP, Guha A, Sdringola S. Frequent diagnostic errors in cardiac PET/CT due to misregistration of CT attenuation and emission PET images: a definitive analysis of causes, consequences, and corrections. J Nucl Med. 2007;48:1112–21.

Impaired Myocardium Regeneration With Skeletal Cell Sheets—A Preclinical Trial for Tissue-Engineered Regeneration Therapy

Shigeru Miyagawa,[1] Atsuhiro Saito,[2] Taichi Sakaguchi,[1] Yasushi Yoshikawa,[1] Takashi Yamauchi,[1] Yukiko Imanishi,[1] Naomasa Kawaguchi,[3] Noboru Teramoto,[4] Nariaki Matsuura,[3] Hidehiro Iida,[4] Tatsuya Shimizu,[5] Teruo Okano,[5] and Yoshiki Sawa[1,6]

Background. We hypothesized that autologous skeletal cell (SC) sheets regenerate the infract myocardium in porcine heart as a preclinical trial.

Methods and Results. The impaired heart was created by implantation of ameroid constrictor on left anterior descending for 4 weeks. SCs isolated from leg muscle were cultured and detached from the temperature-responsive domain-coated dishes as single monolayer cell sheet at 20°C. The following therapies were conducted: SC sheets (SC group, n=5); sham (C group n=5). Echocardiography demonstrated that cardiac performance was significantly improved in the SC group 3 and 6 months after operation (fractional area shortening, 3 months; SC vs. C=49.5±2.8 vs. 24.6±2.0%, $P<0.05$) and left ventricle dilatation was well attenuated in the SC group. Color kinesis index showed that distressed regional diastolic and systolic function in infarcted anterior wall was significantly recovered (SC vs. C=57.4±8.6 vs. 30.2±4.7%, $P<0.05$, diastolic: 58.5±4.5 vs. 35.4±6.6%, $P<0.05$, systolic). Factor VIII immunostains demonstrated that vascular density was significantly higher in the SC group than the C group. And % fibrosis and cell diameter were significantly lower in the SC group. And hematoxylin-eosin staining depicted that skeletal origin cells and well-developed-layered smooth muscle cells were detected in the implanted area. Positron emission tomography showed better myocardial perfusion and more viable myocardial tissue in the distressed myocardium receiving SC sheets compared with the myocardium receiving no sheets.

Conclusions. SC sheet implantation improved cardiac function by attenuating the cardiac remodeling in the porcine ischemic myocardium, suggesting a promising strategy for myocardial regeneration therapy in the impaired myocardium.

Keywords: Cells, Heart failure, Myocardial infarction, Tissue, Transplantation.

(*Transplantation* 2010;90: 364–372)

Despite the recent remarkable progress in medical and surgical treatments for heart failure, end-stage heart failure has been still a major cause of death worldwide. After myocardial infarction, the myocardium is capable of a limited regenerative capacity and no medication or procedure used clinically has shown efficacy in regenerating myocardial scar tissue with functioning tissue. Thus, there is a need for new therapeutics to regenerate damaged myocardium.

Recent developments in tissue engineering show promise for the creation of functional cardiac tissues without the need for biodegradable alternatives for the extracellular matrix (*1*). And we reported that cardiomyocyte sheets have been developed by using temperature-responsive culture dishes and these sheets survived in the back of nude rats and showed a spontaneous contraction over a long period of time (*2*). Recent reports suggested that cardiomyocyte sheets integrated with the impaired myocardium and improved cardiac performance in a rat model of ischemic myocardium (*3*).

This work was supported by a Grant-in-Aid for Scientific Research in Japan.

[1] Division of Cardiovascular Surgery, Department of Surgery, Faculty of Medicine, Osaka University Graduate School of Medicine, Suita, Osaka, Japan.

[2] Medical Center for Translational Research, Osaka University Hospital, Osaka, Japan.

[3] Department of Pathology, School of Allied Health Science, Faculty of Medicine, Osaka University Graduate School of Medicine, Suita, Osaka, Japan.

[4] Department of Investigative Radiology, National Cardiovascular Center Research Institute, Tokyo, Japan.

[5] Tokyo Women's Medical University Institute of Advanced Biomedical Engineering and Science, Tokyo, Japan.

[6] Address correspondence to: Yoshiki Sawa, M.D., Department of Cardiovascular Surgery, Osaka University Graduate School of Medicine, 2-2 Yamada-oka, Suita, Osaka 565-0871, Japan.

E-mail: sawa@surg1.med.osaka-u.ac.jp

S.M. participated in the writing of the paper; A.S. participated in research design; T.S. and Y.Y. participated in data analysis; T.Y., Y.I., N.K., and N.T. participated in the performance of research; N.M., H.I., T.S., T.O., and Y.S. participated in research design.

Received 15 December 2009. Revision requested 2 January 2010.

Accepted 6 May 2010.

ISSN 0041-1337/10/9004-364

DOI: 10.1097/TP.0b013e3181e6f201

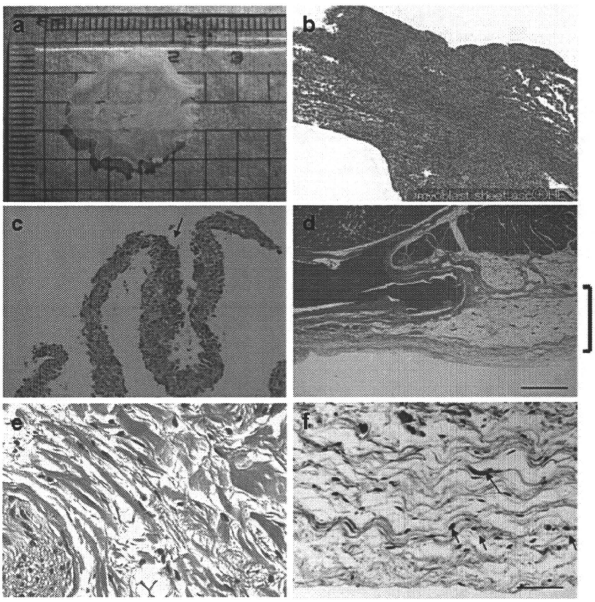

FIGURE 1. Histological characteristics of skeletal cell (SC) sheet. (a) SC sheet detached from the Poly (*N*-isopropylacrylamide)-grafted polystyrene by lowering the temperature. Its size is approximately 3 cm×2 cm^2. (b) Hematoxylin-eosin (H&E) stain; cross-sectional views of SC sheet in vitro. SC sheet demonstrates homogeneous heart-like tissue. (c) Not so many smooth muscle cells were detected in the SC sheets. The *arrow* indicates the smooth muscle cells in the SC sheet. (d) H&E stain revealed that SC sheets attached on the surface of epicardium. *Left square bracket* indicates implanted SC sheets. (e) Oval-shaped cells that showed positive for eosin in cytoplasm were detected in the SC group microscopically in some layers over epicardium. (f) Elastica Masson Goldner showed that oval-shaped cells that supposed to origin from skeletal tissue exist in the transplantation site. *Arrows* indicate oval-shaped cells that suppose to be originated form skeletal tissue.

during the first 30% of the diastolic filling time (LV segmental cavity area expansion during the first 30% of diastole, divided by the segmental end-diastolic LV cavity area expansion, expressed as a percentage). We introduced the use of color kinesis method that displays endocardial motion in real time to evaluate the regional systolic function (*8*).

Histopathology

LV myocardium specimens were obtained 6 months after the SC sheet implantation. Each specimen was fixed with 10% buffered formalin and embedded in paraffin. A few serial sections were prepared from each specimen and stained with hematoxylin-eosin (H&E) stain and elastica Masson-Goldner for histological examination or with Masson's trichrome stain to assess the collagen content.

To label vascular endothelial cells so that the blood vessels could be counted, immunohistochemical staining of factor VIII-related antigen was performed according to a modified protocol. Frozen sections were fixed with a 2% paraformaldehyde solution in phosphate-buffered saline (PBS) for 5 min at room temperature, immersed in methanol with 3% hydrogen peroxide for 15 min, then washed with PBS. The samples were covered with bovine serum albumin solution (DAKO LSAB Kit DAKO CORPORATION, Denmark) for 10 min to block nonspecific reactions. The specimens were incubated overnight with an Enhanced Polymer One-Step Staining (EPOS)-conjugated antibody against factor VIII-related antigen coupled with horseradish peroxidase (DAKO EPOS Anti-Human Von Wille brand Factor/HRP, DAKO, Denmark). After the samples were washed with PBS, they were immersed in diaminobenzidine solution (0.3 mg/mL diaminobenzidine in PBS) to obtain positive staining. Ten different fields at 200× magnification were randomly selected, and the number of the stained vascular endothelial cells in each field was counted under a light microscope. The result was expressed as the number of blood vessels per square millimeter.

The following antibodies against smooth muscle cells and skeletal myosin (slow) were used to evaluate the existence of SCs: primary antibodies, anti-smooth muscle actin (clone 1A4, DAKO) antiskeletal myosin (slow) (clone NOQ7.5.4D, Sigma); secondary antibodies, anti-mouse Ig biotinylate (DAKO).

Picro-sirius red staining for the assessment of myocardial fibrosis or periodic acid-Schiff staining for that of cardiomyocyte hypertrophy was performed as described (*9*).

Positron Emission Tomography Procedure

We performed positron emission tomography (PET) studies on pigs which were transplanted SC sheets and control by using ^{15}0-water and ^{18}F-FDG. The pigs were anesthetized by the introduction of pentobarbital followed by continuous inhalation of propofol (4 mg/kg/hr) and were placed supine on the bed of the scanner. PET was performed using a HEADTOME-III tomograph (Shimadzu, Kyoto, Japan) and data were analyzed as described elsewhere (*10*).

Holter Electrocardiography

To evaluate arrhythmia we used Holter electrocardiography (ECG) for 24 hours. We checked arrhythmia by checking the number of ventricular premature beat after SC sheet implantation in myocardial infarction porcine (n=3).

Data Analysis

Data are expressed as means ± SEM and subjected to multiple analysis of variance (ANOVA) using the StatView 5.0 program (Abacus Concepts, Berkeley, CA). Echocardiographic data were first analyzed by two-way repeated measurement ANOVA for differences across the whole time course, and one-way ANOVA with the Tukey-Kramer posthoc test was used to verify the significant for the specific comparison at each time point. To assess the significance of the differences between individual groups concerning other numeral data, statistical evaluation was performed with an unpaired *t* test. Statistical significance was determined as having a *P* value less than 0.05.

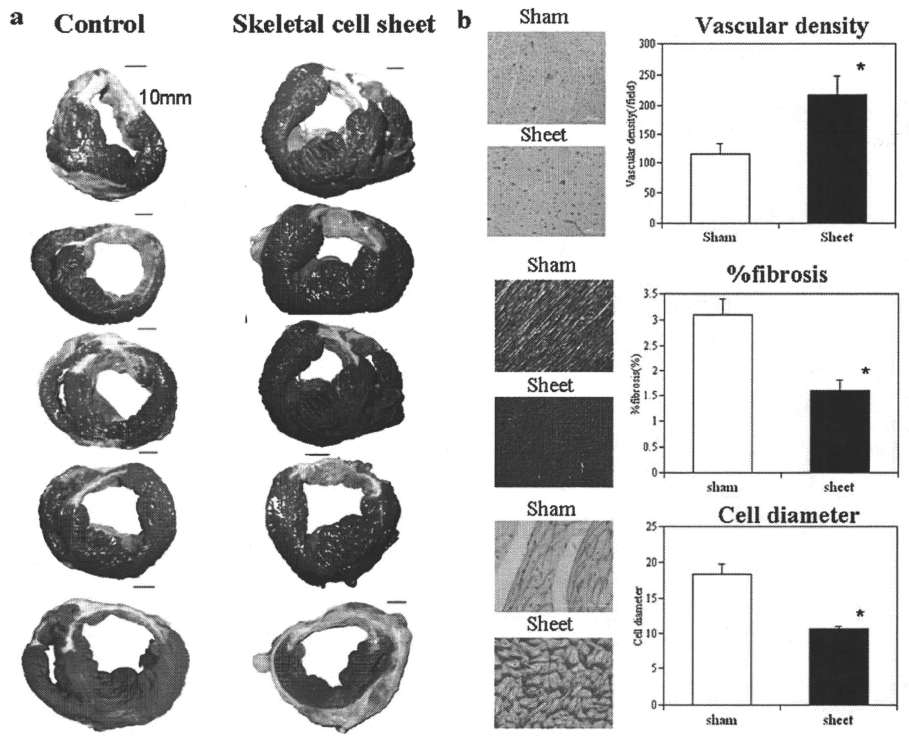

FIGURE 3. Macroscopic images of impaired myocardium receiving skeletal cell (SC) sheets and histological evaluation. (a) In the SC group, the anterior wall has recovered compared with the C group. In the SC group, the short axis area of the left ventricle (LV) is small compared with the C groups. In contrast, the C group shows a dilated LV and the anterior wall is thinner than in the SC groups. (b) Histological evaluation. Vascular density: the SC group showed a significant improvement in vascular density as assessed by immunostaining for the factor VIII-related antigen. *P less than 0.05 vs. C. The ratio of fibrosis-occupied area (% fibrosis) at a site remote from the infarcted heart region: picro-sirius red staining demonstrated that % fibrosis at a site remote from the infarcted heart region was significantly reduced in the SC group compared with the C group. *P less than 0.05 vs. C. The diameter of cardiomyocyte: the diameter of cardiomyocyte is significantly shorter in the SC group than the C group. *P less than 0.05 vs. C.

FIGURE 4. Global functional effects of infarcted myocardium receiving the implant. Global systolic function assessed by the fractional area shortening (FAS) (a) was significantly improved in the skeletal cell (SC) group 3 months after transplantation, and these functional improvements were preserved 6 months after SC sheet implantation. (b) The end-systolic area (ESA) was significantly smaller in the SC group than in the C groups 3 and 6 months after implantation. *P less than 0.05 vs. C, ■: SC sheet, ●: control.

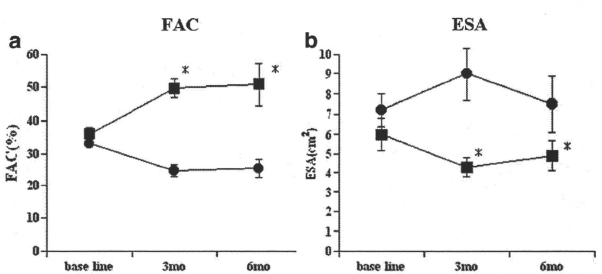

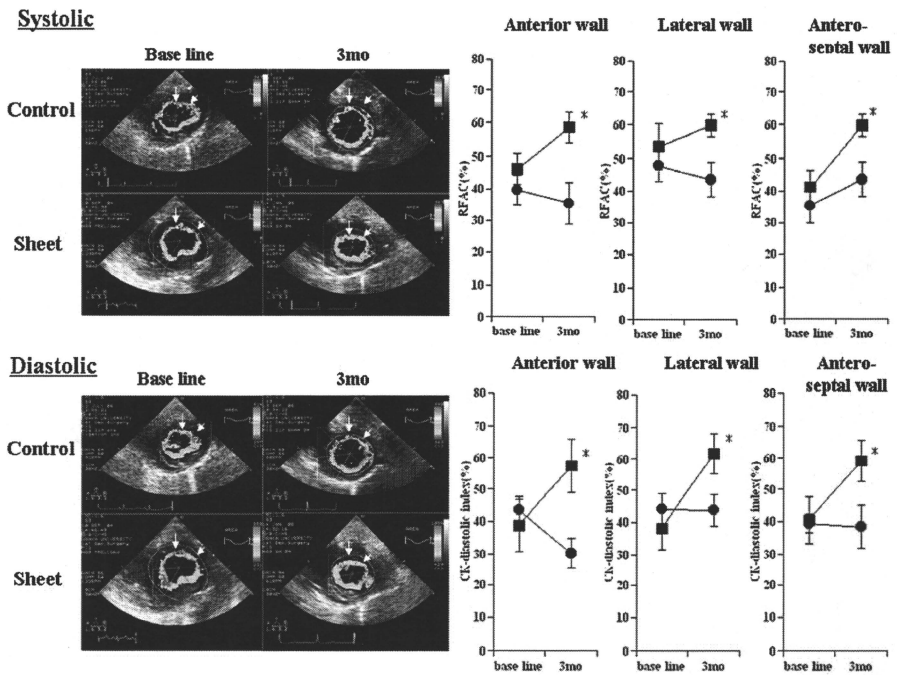

FIGURE 5. Systolic function: regional systolic function was significantly recovered in the skeletal cell (SC) group 3 months after implantation compared with the C group in the anterior, lateral, and anteroseptal wall. *P less than 0.05. Diastolic function: regional dysfunction was significantly recovered in the SC group 3 months after implantation compared with the C group in the anterior, lateral, and anteroseptal wall. Before treatment, diastolic dysfunction was observed in the infarction area of myocardium and the regional delayed relaxation was detected in the remote site of infarction by color kinesis. But this phenomenon was disappeared after SC sheet implantation. *P less than 0.05, ■: SC sheet, ●: control.

FAS (Fig. 4a) in the SC group compared with the C group (SC vs. C=49.5±2.8 vs. 24.6±2.0%, $P<0.05$). These functional improvements were preserved 6 months after implantation (SC vs. C=50.8±6.4 vs. 25.3±2.8%, $P<0.05$). The ESA was significantly smaller in the SC group than in the C group 3 months after the implantation (SC vs. C=4.3±0.5 vs. 9±1.3 cm^2, $P<0.05$) (Fig. 4b). These attenuation of LV dilatation were preserved 6 months after implantation (SC vs. C=4.9±0.8 vs. 7.5±1.4 cm^2, $P<0.05$). During this long-term observation, all SC sheet-treated animals were alive and exhibited no malignant arrhythmia assessed by 24-hour Holter ECG once a week (data not shown).

Before treatment, diastolic dysfunction was observed in the infarction area of myocardium and the regional delayed relaxation was detected in the remote site of infarction by color kinesis. After 3 months after implantation, CK-diastolic index in the lateral (SC vs. C=61.7±6.4 vs. 43.7±4.8%, $P<0.05$), anterior (SC vs. C=57.4±8.6 vs. 30.2±4.7%, $P<0.05$), and anteroseptal (SC vs. C=59±6.6 vs. 38.4±6.6%, $P<0.05$) segment were significantly ameliorated in the SC group compared with the C group, and regional systolic function in transplanted site was significantly improved in the SC group while not in the C groups (SC vs. C: lateral, 59.8±3.3 vs. 43.6±5.4%, $P<0.05$; anterior, 58.5±4.5 vs. 35.4±6.6%, $P<0.05$; anteroseptal, 59.8±3.3 vs. 43.6±5.4%, $P<0.05$), respectively (Fig. 5).

We could detect no ventricular premature beat for 24 hr by the Holter ECG in three myocardial infarction porcine received SC sheets.

Regional Myocardial Blood Flow and Residual Myocardial Tissue

PET study by using ^{15}O-water showed that the myocardial water-perfusable tissue fraction and myocardial blood flow were higher in the anterior wall where SC sheets were implanted compared with the myocardium receiving no sheets. These data depict that myocardial blood flow was better and microcirculation in the infarcted myocardium was preserved in the SC sheets implanted myocardium. PET study by using ^{18}F-FDG revealed that more viable myocardial tis-

14. Li RK, Jia ZQ, Weisel RD, et al. Survival and function of bioengineered cardiac grafts. *Circulation* 1999; 100(suppl II): II-63.
15. Suzuki K, Murtuza B, Beauchamp JR, et al. Role of interleukin-1beta in acute inflammation and graft death after cell transplantation to the heart. *Circulation* 2004; 110(11 suppl 1): II-219.
16. Tanaka H, Kawai H, Tatsumi K, et al. Relationship between regional and global left ventricular systolic and diastolic function in patients with coronary artery disease assessed by strain rate imaging. *Circ J* 2007; 71: 517.
17. Tanaka H, Kawai H, Tatsumi K, et al. Improved regional myocardial diastolic function assessed by strain rate imaging in patients with coronary artery disease undergoing percutaneous coronary intervention. *J Am Soc Echocardiogr* 2006; 19: 756.
18. Moller JE, Hillis GS, Oh JK, et al. Wall motion score index and ejection fraction for risk stratification after acute myocardial infarction. *Am Heart J* 2006; 151: 419.
19. Liu Y, Rajur K, Tolbert E, et al. Endogenous hepatocyte growth factor ameliorates chronic renal injury by activating matrix degradation pathways. *Kidney Int* 2000; 58: 2028.
20. Miyagawa S, Sawa Y, Taketani S, et al. Myocardial regeneration therapy for heart failure: Hepatocyte growth factor enhances the effect of cellular cardiomyoplasty. *Circulation* 2002; 105: 2556.
21. Taniyama Y, Morishita R, Aoki M, et al. Therapeutic angiogenesis induced by human hepatocyte growth factor gene in rat and rabbit hindlimb ischemia models: Preclinical study for treatment of peripheral arterial disease. *Gene Ther* 2001; 8: 181.
22. Li Q, Li B, Wang X, et al. Overexpression of insulin-like growth factor-1 in mice protects from myocyte death after infarction, attenuating ventricular dilation, wall stress, and cardiac hypertrophy. *J Clin Invest* 1997; 100: 1991.
23. Bock-Marquette I, Saxena A, White MD, et al. Thymosin beta4 activates integrin-linked kinase and promotes cardiac cell migration, survival and cardiac repair. *Nature* 2004; 432: 466.

Ann Nucl Med (2010) 24:413–420
DOI 10.1007/s12149-010-0374-x

ORIGINAL ARTICLE

Optimization of transmission scan duration for ^{15}O PET study with sequential dual tracer administration using *N*-index

Nobuyuki Kudomi · Hiroshi Watabe · Takuya Hayashi · Hisashi Oka · Yoshinori Miyake · Hidehiro Iida

Received: 14 October 2009 / Accepted: 4 March 2010 / Published online: 17 April 2010

Abstract
Purpose Cerebral blood flow (CBF), oxygen extraction fraction (OEF) and cerebral metabolic rate of O_2 ($CMRO_2$) can be quantified by PET with the administration of $H_2^{15}O$ and $^{15}O_2$. Recently, a shortening in the duration of these measurements was achieved by the sequential administration of dual tracers of $^{15}O_2$ and $H_2^{15}O$ with PET acquisition and integration method (DARG method). A transmission scan is generally required for correcting photon attenuation in advance of PET scan. Although the DARG method can shorten the total study duration to around 30 min, the transmission scan duration has not been optimized and has possibility to shorten its duration. Our aim of this study was to determine the optimal duration for the transmission scan. We introduced '*N*-index', which estimates the noise level on an image obtained by subtracting two statistically independent and physiologically equivalent images. The relationship between noise on functional images and duration of the transmission scan was investigated by *N*-index.
Methods We performed phantom studies to test whether the *N*-index reflects the pixel noise in a PET image. We also estimated the noise level by the *N*-index on CBF, OEF and $CMRO_2$ images from DARG method in clinical patients, and investigated an optimal true count of the transmission scan.
Results We found tight correlation between pixel noise and *N*-index in the phantom study. By investigating relationship between the transmission scan duration and *N*-index value for the functional images by DARG method, we revealed that the transmission data with true counts of more than 40 Mcounts results in CBF, OEF, and $CMRO_2$ images of reasonable quantitative accuracy and quality.
Conclusion The present study suggests that further shortening of DARG measurement is possible by abridging the transmission scan. The *N*-index could be used to determine the optimal measurement condition when examining the quality of image.

Keywords Transmission scan · PET · O-15 gas · Image quality

N. Kudomi
Department of Medical Physics, Faculty of Medicine, Kagawa University, Mikichou, Kitagun, Kagawa 761-0793, Japan

H. Watabe (✉)
Department of Molecular Imaging in Medicine, Osaka University Graduate School of Medicine, 2-2 Yamadaoka, Suita, Osaka 565-0871, Japan
e-mail: watabe@mi.med.osaka-u.ac.jp

N. Kudomi · H. Watabe · T. Hayashi · H. Iida
Department of Investigative Radiology, Advanced Medical-Engineering Center, National Cardiovascular Center-Research Institute, 5-7-1, Fujishirodai, Suita, Osaka 565-8565, Japan

H. Oka · Y. Miyake
Department of Radiology, National Cardiovascular Center, Hospital, 5-7-1, Fujishirodai, Suita, Osaka 565-8565, Japan

Introduction

Cerebral blood flow (CBF), oxygen extraction fraction (OEF) and cerebral metabolic rate of oxygen ($CMRO_2$) images have facilitated the understanding of the pathophysiological basis of cerebro-vascular disorders, and these images can be quantitatively measured using positron emission tomography (PET) with bolus administrations of ^{15}O-labeled oxygen ($^{15}O_2$) and water ($H_2^{15}O$) [1]. In the conventional three-step method [1–3], these functional

images were measured with separate scans for three tracers of $C^{15}O$ for cerebral blood volume (CBV), $H_2^{15}O$ for CBF and $^{15}O_2$ for $CMRO_2$, and there were additional waiting times between the scans in order to avoid the contamination of the previous tracer on the PET data. Therefore, the measurement process required a relatively long duration of around 1 h in the conventional method. Recently, the duration of the CBF, OEF and $CMRO_2$ measurements was shortened using a dual tracer autoradiography (DARG) method [4]. The DARG method is characterized by sequentially administrating dual tracers of $^{15}O_2$ and $H_2^{15}O$ typically for 3 min interval during a single PET scan. When compared with the conventional three-step method, the DARG method can shorten the total study period to approximately 30 min for the set of CBV, CBF, OEF and $CMRO_2$ measurements while maintaining the image quality and quantitative accuracy.

In order to shorten the examination period even more, one option is to eliminate the CO scan which is used to correct for radioactivity in vascular space [5]. The other is to shorten the duration of the transmission scan, which is required to correct the attenuation of the number of pairs of emitted 511 keV photons in the materials of brain or other, to quantitatively estimate the radio-tracer concentrations. Usually, transmission scan is performed with external ^{68}Ge sources [6, 7]. By prolonging the duration of transmission scan, the accuracy of attenuation correction (AC) will be improved, which results in better quality and accuracy of the functional images although a patient receives additional radiation exposures. In contrast, by shortening the duration of the transmission scan, the functional images might be deteriorated due to lack of statistics. Thus, optimization of transmission scan duration is needed. Because the ^{68}Ge rod sources radioactively decay with a half-life of 270.95 days, the optimal transmission scan duration depends on the radioactivity of the ^{68}Ge source and should be determined by the true transmission scan count. To determine the optimal true count of the transmission scan, quantitative accuracy (bias) and image quality (noise on image) of the CBF, OEF and $CMRO_2$ images must be considered. The quantitative accuracy can be evaluated by comparing two images generated from different transmission scan durations. Noise equivalent counts, NEC, is often used index to evaluate noise in PET image. However, by the NEC, noise propagation from the transmission scan cannot be assessed. Alternatively, to determine the quality of images, one can perform replicated PET measurements and evaluate pixel-wise standard deviation (SD) from these images [8]. Acquiring multiple images, however, are not practical, because measurement conditions such as the administration dose and physiological state cannot be equivalent across replicated measurements.

In this study, in order to evaluate image quality, we introduced an '*N*-index' to define the noise level in an image. The validity of the *N*-index was tested using the Hoffman brain phantom [9]. In order to determine the optimal true count for the transmission scan, the introduced *N*-index was used to evaluate the noise level in the CBF, OEF and $CMRO_2$ images obtained from actual PET data with DARG method for patients with cerebro-vascular disease.

Materials and methods

Phantom studies for validation of *N*-index

It has been reported that the pixel-wise SD of a PET image reconstructed by the filtered backward projection (FBP) method was spatially uniform even in a nonhomogenous region [10]. On the basis of this suggestion, if we obtain two images of the same object with same activity concentration level from two independent scans or procedures, a spatial distribution of pixel values in the subtracted image between those two images has zero mean and its variation is related to the noise level of the images. The *N*-index is defined as the SD of the spatial distribution of the subtracted image.

To verify whether the *N*-index can be used as an index for noise level, the computed *N*-index was compared with the pixel-wise SD value of a PET image obtained from scanning a non-uniform object. We performed a PET experiment using the Hoffman brain phantom [9] filled with $^{18}F_2$ diluted in water. An ECAT EXACT HR (CTI Inc. Knoxville, USA) was used as the PET scanner, and the emission scan acquisition in the 2D mode was repeated every hour. Seven scans were performed. Before the first scan, approximately 207 MBq of $^{18}F_2$ with half-life of 109.8 min, water was injected. Each scan comprised 5 s × 50 frames and the total acquired time was 250 s so that the calculated image count at each location must be almost constant across frames (~0.05% change between adjacent frames and ~3% between the first and last frames). 72 h after the first scan (when the radioactivity of ^{18}F became negligible), two 10-min transmission scans were performed.

Two AC maps were created to correct the attenuation using the data from the two 10-min transmission scans. Using these AC maps, two dynamic images were reconstructed by employing the FBP method from the same sinogram data. Corrections for randoms, dead time, scatters, and radioactivity decay to the start time of the first scan were applied, and the Gaussian filter with a filter width of 7 mm was used. For the obtained images, we defined the *j*th pixel value as $x_{i,j}^{n,k}$ with the *k*th frame ($k = 1, 2, \ldots, 50$) at *n*th scan

($n = 1, 2, \ldots, 7$) with ith AC map ($i = 1, 2$). Each image had a matrix size of 128 × 128 × 47 with a pixel size of 1.8 × 1.8 × 3.38 mm.

The pixel-wise SD images ($s^n_{i,j}$) were computed from all the 50 frames of the dynamic images as;

$$s^n_{i,j} = \mathrm{SD}_{k=1,\ldots,50}[x^{n,k}_{i,j}] \quad (1)$$

where, $\mathrm{SD}_{k\in K}[y_k]$ is defined as a standard deviation of y_k over K.

We calculated N-indices from two datasets to test equivalence of N-index to pixel-wise SD when amount of data change in terms of either scan duration or activity concentration as: (a) one frame data of duration 5 s and (b) 25 frames data of duration 125 s. For the dataset (a), a subtracted image ($I^{n,5s}_j$) was created by subtracting the 24th frame data with the first AC map from the 25th frame data with the second AC map as:

$$I^{n,5s}_j = x^{n,25}_{1,j} - x^{n,24}_{2,j}. \quad (2)$$

The reason that we selected the 24th and 25th frames for the subtraction was to minimize the influence of physical decay in the pixel value. For the dataset (b), even-numbered frames with the first AC map and odd-numbered frames with the second AC map were summed in order to obtain two independent (but must be identical in terms of the radioactivity count at each location) images. By subtracting the two images, the subtracted image was created as:

$$I^{n,125s}_j = \frac{1}{25}\sum_{k\in\mathrm{odd}} x^{n,k}_{1,j} - \frac{1}{25}\sum_{k\in\mathrm{even}} x^{n,k}_{2,j}. \quad (3)$$

The reason that we summed the frames alternately was to minimize the influence of physical decay in the pixel value. The subtracted image has a mean value that is approximately and uniformly zero.

A circular region of interest (ROI) (10.7 cm in diameter, 3620 pixels) was placed in the brain region on a slice at the level of thalamus. The mean SD value (M^n_{SD}) of $s^n_{i,j}$ and the N-index ($\mathrm{NI}^{n,t}$) of $I^{n,t}$ inside the ROI were calculated and compared.

Subjects and PET procedure

For the CBF and $CMRO_2$ measurements, we performed a series of PET scans on six human subjects with cerebrovascular disease ($n = 6$, age = 69 ± 3 years, body weight = 64 ± 4 kg). The DARG approach [4, 11] was employed to compute the CBF and $CMRO_2$ images. An ECAT EXACT 47 (CTI Inc. Knoxville, USA), equipped with three rotating ^{68}Ge–^{68}Ga rod sources was used as the PET scanner. The PET procedures were approved by the ethics committee of the National Cardiovascular Center.

Transmission scans with multiple frames (60 s × 9 frames and 30 s × 2 frames) were performed for 10 min. After the transmission scan, a 4-min static emission scan along with $C^{15}O$ administration was performed. Subsequently, a dynamic DARG $H_2{}^{15}O$–$^{15}O_2$ scan [4] was started with the sequential administration of gaseous $^{15}O_2$ (3000 MBq, 1-min inhalation) followed by $H_2{}^{15}O$ (1110 MBq, intra-venous injection into the right brachial vein) administration after 6 min. The DARG scan sequence comprised 10 s × 6 frames, 20 s × 6 frames, 30 s × 4 frames, 10 s × 4 frames, 5 s × 10 frames and 15 s × 2 frames. All data were acquired in the 2D mode with extended septa.

To obtain the arterial input function, a catheter was inserted into the brachial artery, and blood was withdrawn at a flow rate of 4 ml/min during each emission PET scan. The arterial blood time activity curve (TAC) was continuously monitored using a GSO input function monitor [12].

Data processing

From the multi-frame transmission data with 11 frames, two sets for 30, 60, 120, 180, 240 and 300 s were generated by adding the frames and avoiding duplications. In addition, the sum of the transmission data with a duration of 600 s was obtained. On the basis of the obtained transmission data and the blank scan data, 13 AC maps were generated defined as AC^t_i, where $i = 1, 2$ (index of the sets), and $t = 30, 60, 120, 180, 240, 300$ s (transmission data time duration) and AC^{600s}_1.

Along with detector normalization, the static images for the $C^{15}O$ scan and the dynamic image for the $^{15}O_2$–$H_2{}^{15}O$ emission scan sinograms were corrected for dead time and radioactive decay in each frame. Tomographic images were reconstructed using these corrected sinograms obtained by the FBP method with 7-mm Gaussian filtering. AC was applied to the $C^{15}O$ static image using the AC map obtained from the 600-s transmission data, (i.e., AC^{600s}_1), and to the $^{15}O_2$–$H_2{}^{15}O$ dynamic image using all the generated AC map data of AC^t_i. Thus, 13 dynamic images were obtained. The pixel value was defined as $x^k_{j,(i,t)}$ for jth pixel value with kth frame using AC^t_i. A scatter correction was also applied. The reconstructed dynamic images had a matrix size 128 × 128 × 47 with a pixel size of 1.8 × 1.8 × 3.38 mm.

The following three steps were employed to sum up a part of the reconstructed dynamic image for the $^{15}O_2$–$H_2{}^{15}O$ scan during each oxygen (180 s from the start of oxygen inhalation, indicated as: $k \in O_2$) and water (120 s from the increase in the brain tissue TAC, indicated as: $k \in H_2O$) phase. First, all the frames were summed as: $\sum^{k\in O_2,\mathrm{all}} x^k_{j,(1,t)}$ and $\sum^{k\in H_2O,\mathrm{all}} x^k_{j,(1,t)}$. Second, all the even-numbered frames

were summed as: $\sum^{k\in O_2,\text{even}} x^k_{j,(2,t)}$ and $\sum^{k\in H_2O,\text{even}} x^k_{j,(2,t)}$. Lastly, all the odd-numbered frames were summed as: $\sum^{k\in O_2,\text{odd}} x^k_{j,(1,t)}$ and $\sum^{k\in H_2O,\text{odd}} x^k_{j,(1,t)}$. We assumed two images summed with even- and odd-numbered frames are physiologically and quantitatively equivalent and statistically independent.

Arterial blood TACs were corrected for radioactivity decay and dispersion ($\tau = 4$ s) [4, 13, 14] and delay [3, 4, 15] further, the $^{15}O_2$ and $H_2^{15}O$ contents were separated [11]. The obtained $^{15}O_2$ and $H_2^{15}O$ arterial TACs were used as the water and oxygen input functions as $A_W(t)$ and $A_O(t)$, respectively.

Sets of CBF, OEF and $CMRO_2$ images were generated using the DARG approach as described previously [4] by using a set of summed images in both the oxygen and water phases ($\sum^{k\in O_2,\rho} x^k_{j,(1,t)}$ and $\sum^{k\in H_2O,\rho} x^k_{j,(1,t)}$, where ρ indicates the rule of sum, i.e., all, even or odd), $^{15}O_2$ and $H_2^{15}O$ input functions [$A_W(t)$ and $A_O(t)$] and cerebral blood volume (CBV) image that was obtained from the $C^{15}O$ scan data [3, 4]. This procedure was repeated for all sets of images and the functional images for jth pixel were obtained as: $CBF^{\rho}_{j,(i,t)}$, $OEF^{\rho}_{j,(i,t)}$ and $CMRO2^{\rho}_{j,(i,t)}$, where indices (i, t) are same as those for AC, and ρ is the rule of sum.

Dependency of quantitative CBF/OEF/$CMRO_2$ accuracy on the transmission true counts

An ROI was placed on the frontal, temporal and parietal cortical region (5000–10000 pixels) of the image and the CBF, OEF and $CMRO_2$ values were extracted from all the datasets. The mean of these extracted values was expressed as the percent difference between the values obtained from the functional images computed with AC^t_1 and with AC^{600s}_1 for all datasets obtained from the emission data as:

$$\frac{R\left[\text{Func}^{\text{all}}{}_{j,(1,t)}\right] - R\left[\text{Func}^{\text{all}}_{j,(1,600s)}\right]}{R\left[\text{Func}^{\text{all}}_{j,(1,600s)}\right]} \times 100\% \quad (4)$$

where R indicates mean pixel value inside the ROI and Func indicates either CBF, OEF or $CMRO_2$.

Dependency of CBF/OEF/$CMRO_2$ image quality on the transmission true counts

Subtracted images were created by subtracting the functional images between even- and odd-numbered frames as;

$$I^{\text{Func}}_{j,t} = \text{Func}^{\text{even}}_{j,(1,t)} - \text{Func}^{\text{odd}}_{j,(2,t)} \quad (5)$$

for the jth pixel. The N-index in the ROI, placed on the frontal, temporal and parietal cortical region as above, for these subtracted images were calculated as:

$$\text{NI}^t_{\text{Func}} = \text{SD}_{j\in\text{ROI}}\left[I^{\text{Func}}_{j,t}\right]. \quad (6)$$

The obtained N-indices were expressed as a function of the total true count of the transmission scan data.

Results

Phantom studies for validation of N-index

Figure 1 shows representative slices of the obtained images of mean, SD, and subtraction. The later scan has more noise due to count statistics, which can be observed in SD image and the subtracted images in Fig. 1. Despite the difference in the activity distribution, the SD image was almost uniform. The relationship between the mean value of the SD image (M_{SD}) and N-index (NI) in the same ROI

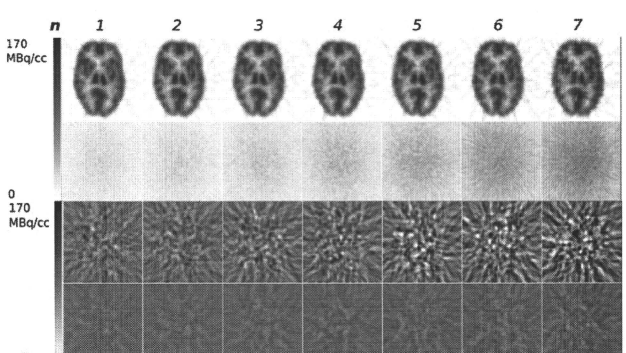

Fig. 1 Representative slices of the reconstructed images obtained from the phantom studies. The *first row* is averaged image, the *second row* is SD image, the *third row* is the subtracted image for the dataset (a), and the *fourth row* is the subtracted image for the dataset (b). *Each column* corresponds the images from nth scan (total seven scans)

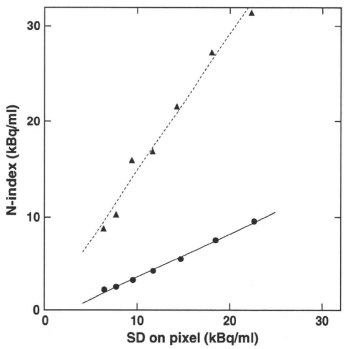

Fig. 2 The relationship between the mean SD value and *N*-index obtained from the subtracted image with the same ROI region of the brain phantom. The regression line was expressed as $y = 1.44x - 0.331$ (kBq/ml) ($r = 0.99$, $n = 7$). and $y = 0.47x - 1.29$ (kBq/ml) ($r = 0.99$, $n = 7$), for 5 s (*closed triangle*) and 125 s (*closed circle*) in calculating *N*-index, respectively

is shown in Fig. 2. The regression line is expressed as $NI = 1.44M_{SD} - 0.331$ (kBq/ml) ($r = 0.99$) and $NI = 0.47M_{SD} - 1.285$ (kBq/ml) ($r = 0.99$), where r is correlation coefficient, for the subtracted images obtained from the 5- and 125-s data, respectively. The results shown in Figs. 1 and 2 support the assumption that the SD of the pixel value is uniform in a non-homogeneous image that was reconstructed using the FBP method. Furthermore, the present *N*-index was correlated with the SD and could be employed to compare the image qualities.

Dependency of quantitative CBF/OEF/$CMRO_2$ accuracy on the transmission true counts

Figure 3 shows the percent difference in the CBF (a), OEF (b) and $CMRO_2$ (c) values when compared with those computed using the 10-min AC map. The results show that the quantitative values obtained during the CBF, OEF and $CMRO_2$ measurements are almost identical, namely, difference was <5% to those obtained when AC was performed using the transmission data containing true counts more than 40 Mcounts.

Dependency of the CBF/OEF/$CMRO_2$ image quality on the transmission true counts

Figure 4 shows the *N*-indices in the CBF (a), OEF (b) and $CMRO_2$ (c) images, as a function of the number of true counts of the transmission data. The present results show that the qualities of the CBF, OEF and $CMRO_2$ images

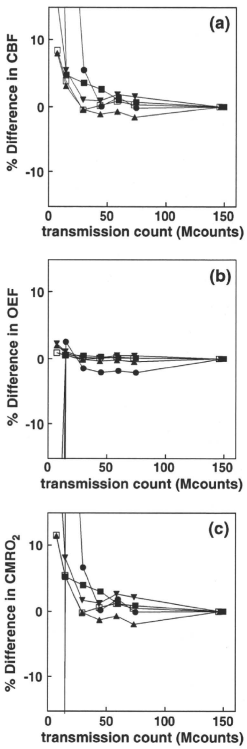

Fig. 3 Percent difference in the CBF, OEF and $CMRO_2$ values when compared with those obtained from the 10-min transmission data, as a function of the true counts of the transmission data. Each type of *symbol* corresponds to each subject ($n = 6$). The indicated values were extracted from the ROI in the frontal, parietal and temporal cortex regions

were almost equal to those in which the true counts of the transmission data used exceeded 40 Mcounts.

Discussion and conclusion

Our purpose of this study was to shorten the transmission scan duration for ^{15}OPET study with DARG measurement. By evaluating bias and noise on the functional images of the CBF, OEF and $CMRO_2$ due to noise in transmission data, optimal transmission true count in DARG measurement was

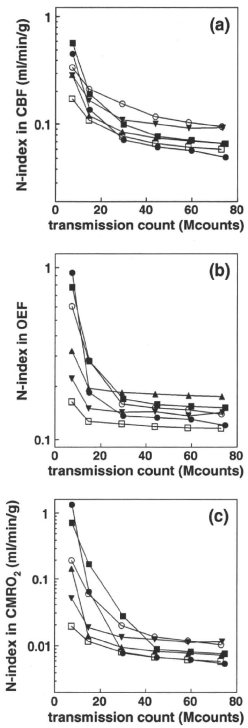

Fig. 4 The *N*-indices for the CBF, OEF and $CMRO_2$ images that were obtained from various true counts of the transmission data as a function of the true counts of the transmission data. Each type of *symbol* corresponds to each subject ($n = 6$). The *symbols* used and ROI are the same as that used for Fig. 3

determined. We found 40 Mcounts of the true count in the transmission scan was optimal, and consequently, we were able to shorten the total duration of the DARG examination.

We introduced the *N*-index to compare the noise level on inhomogeneous functional images. The benefit of using *N*-index is that by one index number, one can characterize the noise in functional image derived from PET data and DARG measurement which have complex noise propagations from several error sources. The validity of the *N*-index was tested in the phantom study. We found tight correlation between pixel noise and the *N*-index.

The present result using the brain phantom supported the assumption that the SD of a pixel value was spatially uniform even in a non-homogeneous region of an FBP reconstructed image (Fig. 1). Furthermore, the regression line between the SD value from the statistically obtained SD image and the *N*-index from the subtracted image for 5- and 125-s data were highly correlated ($r = 0.99$) (Fig. 2). The slope for 5-s data was approximately $\sqrt{2}$, where the SD of the image obtained by subtraction of two 5-s data (statistically corresponding to 10 s) could be expected to be $\sqrt{2}$ greater than that of the original image. For 125-s data, 1/5 of statistical noise compared to 5-s data is expected. However, *N*-index for 125-s data overestimated in 18% in average than expected. One possible reason of this overestimation is influence of inhomogeneity of the reconstructed image. Therefore, the *N*-index cannot be used to estimate absolute noise level in the image, but the *N*-index is still valid for study which compares relative noise levels among multiple images.

Using the *N*-index, we examined the change of image quality in the CBF, OEF and $CMRO_2$ as the noise level based on the change in the true counts of the transmission data. One of the advantages using the *N*-index is that it allows us to compare the noise level of non-uniform images such as that of the brain, using the data obtained by ordinal PET scan procedure. In order to investigate the noise level of the PET images using parameters other than the *N*-index, the PET scans must be replicated for a human subject. However, this appears unlikely due to the excessive radiation dose that would need to be administered to the subject. Furthermore, it might be quite hard to maintain the equivalent measurement conditions such as the radiation dose, as well as the physiological conditions of the subjects.

In this study, two implicit conditions were assumed: the SD on pixel value is uniform for the targeted region and odd-and even-numbered frames have the same statistical properties. The condition of uniform distribution of the SD on the functional image might not be microscopically fulfilled due to nature of nonlinearity of DARG method. However, in global, noise on the reconstructed image could be linearly propagated to the functional image and we considered this assumption was valid for computing the *N*-index. The *N*-index can be applied to other cases such as a variety of tracers and organs in order to examine the image quality as far as those conditions are satisfied. It should be noted that the CBF and $CMRO_2$ parametric images are required to be assessed quantitatively [16], thus the present study was validated with images reconstructed by FBP method. Limitation of the present method is that the *N*-index may not be applied to images such as those reconstructed by the maximum likelihood expectation maximization based algorithm, because the uniformity of SD across pixels is not guaranteed. However, a similar procedure of the present method still has possibility to be

applied, if, for example, coefficient of variation is uniform across pixels.

When *N*-index was estimated from two images with either emission or transmission data being common, the variation on image can be calculated as a sum of each variation and subtraction of covariance, canceling effect of noise from common data. Consequently, the *N*-index only reflects noise on either transmission or emission data. Thus, we estimated *N*-index by subtracting fully independent images. The validity of *N*-index could be tested in the phantom study using common transmission data; however, we still computed *N*-index using fully independent images, because the test should be done in the same conditions as the experimental study.

The present results showed that poor count statistics in transmission scanning resulted in significant bias in quantitative values of CBF, OEF and $CMRO_2$. As has been mathematically described [17], AC factor, i.e. blank/transmission is biased by factor of $(1 + 1/m)$, where m is a transmission count on a corresponding pixel. Therefore, the poorer the transmission scan count is, the higher the AC factor becomes. In view of image quality, noise in transmission data influences functional image as shown in Fig. 4. On the other hand, as indicated in Fig. 4, extra longer transmission scan gains no statistical benefit. The optimized transmission scan duration will be determined by relative noise level of the transmission data against the emission data.

In this paper, we used fixed duration of 600 s of the transmission scan for CO image, assuming little effect of noise on CO image. One reason for this assumption is that 50% error in CBV value derives around only 3% error in OEF and $CMRO_2$ images [4], suggesting 50% noise on CBV image resulting only 3% noise on OEF and $CMRO_2$ images. As shown in Fig. 4, the degree of noise on the OEF and $CMRO_2$ images are around 20–25%, and the level of noise is quite high compared to level of noise from CBV image.

Motion of subject, during a scan, could be a problem to calculate *N*-index. However, movement of a subject during a scan affects both the odd-and even-numbered frames simultaneously, and thus the statistical properties between two summed images will stay the same. Thus, motion of a subject during a scan might not be that critical with regards to the *N*-index, as far as the motion does not deteriorate the image used to assess the function of the targeted organ.

The comparison of the *N*-indices between subjects or between different functional images cannot be performed because the *N*-indices offer information of relative noise level but not absolute noise. Thus, a meaningful comparison can be made between images of the same subject and of the same cerebral function (such as CBF and $CMRO_2$).

It is generally accepted that accurate ACs require transmission scanning using external sources [6, 7], although there are excellent techniques designed to shorten or eliminate the transmission scan duration, such as the transmission-data-based segmented method for the AC map [18, 19] or the emission-based AC map calculation [20]. The present approach might be applicable to investigate the noise level in segmented or emission-based methods, which should enable us to further shorten the duration of a PET examination.

Boellaard et al. demonstrated the relationship between the transmission scan counts and phantom diameter, and they found that this relationship did not restrict the application of the count-based transmission scans for correcting the reduction in the rod source strength [21]. However, they indicated that when the subject is extremely small, a transmission scan based on an acquired number of true counts should not be applied. This is because the counts for lines of response not passing through the subject would increase. Further studies are required to determine the optimal examination conditions for such situations.

We found that the true counts of the transmission data exceeding 40 millions (corresponds to 3 min scan in this study) were appropriate for the CBF, OEF and $CMRO_2$ measurement by DARG method in terms of both quantitative accuracy and image quality, consequently we can shorten the examination duration for obtaining those images. Conventional DARG measurement in clinical study uses 10 min of transmission scan, while 9 min of emission scan of dual tracers of $^{15}O_2$ and $H_2^{15}O$, in addition to 4 min of $C^{15}O$ scan [22]. If one can shorten the transmission scan to 3 min, total scan duration is 16 min (30% reduction). Currently, another $C^{15}O$ scan for CBV correction with regards to the assessment of CBF, OEF and $CMRO_2$ is still required, an additional mathematical formulation strategy, like the basis function method [23] could eliminate this requirement [5].

In conclusion, we determined the required transmission true count that maintains the quantitative accuracy and image quality for PET studies with $H_2^{15}O$ and $^{15}O_2$. According to our results, the total study duration could be minimized by shortening the transmission scan. Although the obtained results in the present study were measurement condition specific, the *N*-index could be used to determine PET scanning procedures.

Acknowledgments The authors would like to thank Ms Atra Ardakani for her invaluable help on preparing this article. The authors gratefully acknowledge the staff of the Department of Nuclear Medicine, Hospital and the Department of Investigative Radiology, Research Institute, National Cardiovascular Center. The present work was supported by the Program for Promotion of Fundamental Studies in Health Science of the Organization for Pharmaceuticals and